Network analysis reveals strongly localized impacts of El Niño

Jingfang Fan[a,1], Jun Meng[a,b,1], Yosef Ashkenazy[b,2], Shlomo Havlin[a], and Hans Joachim Schellnhuber[c,d,2]

[a]Department of Physics, Bar-Ilan University, Ramat-Gan 52900, Israel; [b]Department of Solar Energy & Environmental Physics, Blaustein Institutes for Desert Research, Ben-Gurion University of the Negev, Midreshet Ben-Gurion 84990, Israel; [c]Potsdam Institute for Climate Impact Research, 14412 Potsdam, Germany; and [d]Santa Fe Institute, Santa Fe, NM 87501

Contributed by Hans Joachim Schellnhuber, June 1, 2017 (sent for review January 23, 2017; reviewed by Dirk Helbing and Yochanan Kushnir)

Climatic conditions influence the culture and economy of societies and the performance of economies. Specifically, El Niño as an extreme climate event is known to have notable effects on health, agriculture, industry, and conflict. Here, we construct directed and weighted climate networks based on near-surface air temperature to investigate the global impacts of El Niño and La Niña. We find that regions that are characterized by higher positive/negative network "in"-weighted links are exhibiting stronger correlations with the El Niño basin and are warmer/cooler during El Niño/La Niña periods. In contrast to non-El Niño periods, these stronger in-weighted activities are found to be concentrated in very localized areas, whereas a large fraction of the globe is not influenced by the events. The regions of localized activity vary from one El Niño (La Niña) event to another; still, some El Niño (La Niña) events are more similar to each other. We quantify this similarity using network community structure. The results and methodology reported here may be used to improve the understanding and prediction of El Niño/La Niña events and also may be applied in the investigation of other climate variables.

climate | dynamic network | ENSO

More than a decade ago, networks became the standard framework for studying complex systems (1–5). In recent years, network theory has been implemented in climate sciences to construct "climate networks." These networks have been used successfully to analyze, model, understand, and even predict climate phenomena (6–16). Specific examples of climate network studies include the investigation of the interaction structure of coupled climate subnetworks (17), the multiscale dependence within and among climate variables (18), the temporal evolution and teleconnections of the North Atlantic Oscillation (19, 20), the finding of the dominant imprint of Rossby waves (21), the optimal paths of teleconnection (22), the influence of El Niño on remote regions (8, 23, 24), the distinction of different types of El Niño events (25), and the prediction of these events (15, 16). A network is composed of nodes and links; in a climate network, the nodes are the geographical locations, and the links are the correlations between them. The "strength" of the links is quantified according to the strength of the correlations between the different nodes (21, 26, 27).

El Niño is probably the strongest climate phenomenon that occurs on interannual time scales (28, 29). El Niño refers to the warming of the central and eastern equatorial Pacific Ocean by several degrees ($^\circ$C). La Niña is the cooling of sea surface temperatures (SSTs) in the eastern tropical Pacific Ocean. La Niña usually follows an El Niño event, but not always; the overall phenomenon is referred to as El Niño-Southern Oscillation (ENSO). This cycle occurs every 3–5 y with different magnitudes. There are several indices that quantify the El Niño activity, including the Niño 3.4 Index, the Southern Oscillation Index (SOI) (see, e.g., ref. 30), and the Oceanic Niño Index (ONI), which is the National Oceanic and Atmospheric Administration's (NOAA) primary indicator for monitoring El Niño and La Niña. ONI is the running 3-mo mean SST anomaly for the Niño 3.4 region (i.e., $5^\circ N - 5^\circ S$, $120^\circ - 170^\circ W$); here, we refer to this region as the El Niño Basin (ENB). When the ONI is $>0.5^\circ$C for at least five consecutive months, the corresponding year is considered to be an El Niño year. The higher the ONI is, the stronger the El Niño. Similarly, La Niña is determined to occur when the ONI drops below the -0.5°C anomaly for at least five consecutive months. Presently, we have just undergone one of the strongest El Niño events since 1948 (31, 32).

The El Niño phenomenon strongly affects human life. It can lead to warming, enhanced rain in some regions and droughts in other regions (33), decline in fishery, famine, plagues, even increases in the risks of political and social unrest, and economic changes through globally networked system (34). Global maps of the influence of El Niño had been constructed in ref. 35. The climate network approach has been found to be useful in improving our understanding of El Niño (8, 23–25) and in forecasting it (15, 16). However, that approach has not been developed and applied to study systematically the global impact of El Niño, and that is what we try to achieve in quantitative terms here. We construct the climate network by using only directed links from the ENB to regions outside the ENB (which we call here "in"-links). The constructed in-weighted climate network enables us not only to obtain a map of the global impacts of a given El Niño event, but also to study the impacts of El Niño in specific regions, including North America (36), Australia (37–41), South Africa (42), southern South America (43), Europe (44), and the tropical North Atlantic (45).

In the present study, we identify warming and cooling regions that are influenced by the ENB by measuring each node's strength according to the weights of its links "coming" from the ENB. We find that during El Niño/La Niña, a large fraction of the globe is not influenced by the events, but the regions that are influenced are significantly more affected by the ENB than in normal years. Our findings support the recent sugges-

Significance

El Niño, one of the strongest climatic phenomena on interannual time scales, affects the climate system and is associated with natural disasters and serious social conflicts. Here, using network theory, we construct a directed and weighted climate network to study the global impacts of El Niño and La Niña. The constructed climate network enables the identification of the regions that are most drastically affected by specific El Niño/La Niña events. Our analysis indicates that the effect of the El Niño basin on worldwide regions is more localized and stronger during El Niño events compared with normal times.

Author contributions: Y.A., S.H., and H.J.S. designed research; J.F. and J.M. performed research; J.F. and J.M. analyzed data; and J.F., J.M., Y.A., S.H., and H.J.S. wrote the paper.

Reviewers: D.H., ETH Zurich; and Y.K., Columbia University.

The authors declare no conflict of interest.

[1]J.F. and J.M. contributed equally to this work.

[2]To whom correspondence may be addressed. Email: ashkena@bgu.ac.il or john@pik-potsdam.de.

This article contains supporting information online at www.pnas.org/lookup/suppl/doi:10.1073/pnas.1701214114/-/DCSupplemental.

tion that the climate structure becomes well-confined in certain localized regions during a fully developed El Niño event. This phenomenon is evident by inspecting the emergent teleconnections between the ENB and localized regions. Such a large-scale cooperative mode helps us to forecast El Niño events (15, 16). Our results also indicate that the El Niño/La Niña events influence different regions with different magnitudes during different events; still, by determining the network community structure, our results suggest that similarities exist among some of the El Niño (La Niña) events. We find here that the impact of El Niño is very variable and that it is localized and strong during El Niño events; we quantify this variability and the intensity effect and found, using a directed and weighted network, that it is strongly related to El Niño.

Our evolving climate network is constructed from the global daily near-surface (1000 hPa) air temperature fields of the National Center for Environmental Prediction/National Center for Atmospheric Research (NCEP/NCAR) reanalysis dataset (46); see the *SI Appendix* for the analysis and results based on the European Center for Medium-Range Weather Forecasts Interim Reanalysis (ref. 47 and *SI Appendix*). The spatial (zonal and meridional) resolution of the data are $2.5^\circ \times 2.5^\circ$, resulting in $144 \times 73 = 10512$ grid points. The dataset spans the time period between January 1948 and April 2016. (Because for each window $365 + 200$ days' daily data are used, and the newest data we can obtain is until May 6, 2016, so Φ^y is terminated at the 11th window of 2014.) To avoid the strong effect of seasonality, we subtract the mean seasonal cycle and divide by the seasonal SD for each grid point time series. The overall analysis is based on a sequence of networks, each constructed from time series that span 1 y.

The nodes (grid points) are divided into two subsets. One subset includes the nodes within the ENB (57 nodes) and the other the nodes outside the ENB (10455 nodes). For each pair of nodes, i and j, each from a different subset, respectively, the cross-correlation between the two time series of 365 d is calculated,

$$C^y_{i,j}(\tau) = \frac{\langle T_i(d)\, T_j(d-\tau)\rangle - \langle T_i(d)\rangle \langle T_j(d-\tau)\rangle}{\sigma_{T_i(d)} \sigma_{T_j(d-\tau)}}, \quad [1]$$

where $\sigma_{T_i(d)}$ is the SD of $T_i(d)$, $\tau \in [0, \tau_{max}]$ is the time lag, with $\tau_{max} = 200$ d, y indicates the starting date of the time series with 0 time shift, and $C^y_{i,j}(-\tau) \equiv C^y_{j,i}(\tau)$. We then identify the value of the highest peak of the absolute value of the cross-correlation function and denote the corresponding time lag of this peak as $\theta^y_{i,j}$. The sign of $\theta^y_{i,j}$ indicates the direction of each link; that is, when the time lag is positive ($\theta^y_{i,j} > 0$), the direction of the link is from i to j. Below, we focus on the overall effect of the ENB on regions (grid points) outside this region and thus refer to the links directed from the ENB to a grid point j as in-links to grid point j (24). We only consider in-links with time lag shorter than ~5 mo ($|\theta^y_{i,j}| \le 150$ d) as we focus on the influence of El Niño on the rest of the world on seasonal time scales. Examples of in-links over different regions are shown in Fig. 1 *A* and *B*, and the cross-correlation function of these typical links are presented in *SI Appendix*, Fig. S4. Below, we elaborate on the impacts of El Niño in some of these regions. The link weights are determined by using $C^y_{i,j}(\theta)$, and we define the strength of the link as

$$W^y_{i,j} = \frac{C^y_{i,j}(\theta) - \text{mean}(C^y_{i,j}(\tau))}{\text{std}(C^y_{i,j}(\tau))}, \quad [2]$$

where "mean" and "std" are the mean and SD of the cross-correlation function, respectively (21, 22). We construct networks based on both $C^y_{i,j}(\theta)$ and $W^y_{i,j}$, and these are consistent with each other. See Fig. 1 *A* and *C* for El Niño and Fig. 1 *B* and *D* for La Niña (details are below).

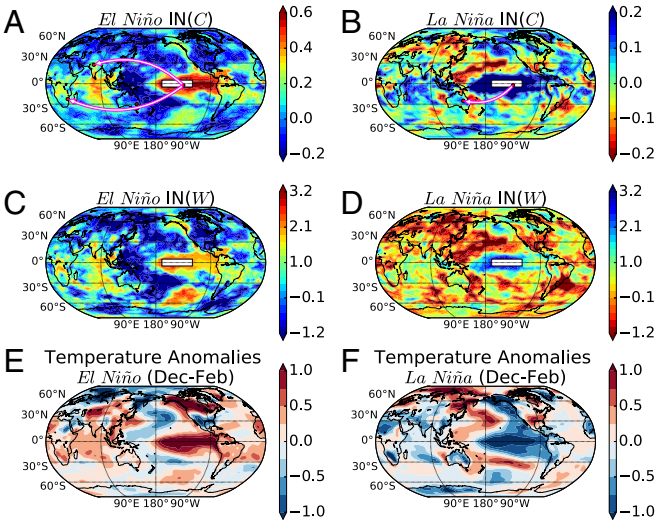

Fig. 1. (*A* and *C*) In-weight maps (using *C* and *W*) for El Niño events. (*B* and *D*) In-weight maps (using *C* and *W*) for La Niña events. (*E* and *F*) Mean winter (December–February) temperature anomalies during El Niño and La Niña. The arrows in *A* indicate two examples of in-links (El Niño impact), outgoing from ENB, to (*i*) Chicualacuala in Mozambique and (*ii*) Rambaxpura in India. The arrow in *B* indicates another example of in-links, outgoing from ENB (La Niña impact) to (*iii*) Jundah in Australia, respectively. The flat white rectangle in *A*–*D* represents the Niño 3.4 region ($5^\circ N - 5^\circ S$, $120^\circ - 170^\circ W$).

The adjacency matrix of a climate network is defined as

$$A^y_{i,j} = (1 - \delta_{i,j}) H(\theta^y_{i,j}), \quad [3]$$

where $H(x)$ is the Heaviside step function ($H(x \ge 0) = 1$ and $H(x < 0) = 0$). The in and "out" degrees of each node are defined as $I^y_i = \sum_j A^y_{j,i}$, $O^y_i = \sum_j A^y_{i,j}$, respectively, quantifying the number of links into a node or out from a node. We define the total in-weights of each node outside the ENB as the sum of the weights of its in-links, using $C^y_{j,i}$ and $W^y_{j,i}$:

$$\text{IN}(C^y_i) = \sum_{j \in ENB} A^y_{j,i} C^y_{j,i}(\theta),$$
$$\text{IN}(W^y_i) = \sum_{j \in ENB} A^y_{j,i} W^y_{j,i}. \quad [4]$$

Larger (smaller) positive (negative) values of $\text{IN}(C^y_i)$ and $\text{IN}(W^y_i)$ reflect stronger (weaker) warming (cooling) due to the impact of the ENB. If there are no in-links for a node, both the in-degree and in-weights are zero, indicating no impact of the ENB.

Based on the ONI, we divide the 68 record years into El Niño, La Niña, and normal years. For simplicity, we only consider moderate and strong El Niño/La Niña events with $|\text{ONI}| > 1^\circ$C. For each event, we consider the time series from July 1 preceding the event to June 30 of the next year, to cover the whole range of one El Niño/La Niña period (48). (The year is centered on the Northern Hemisphere winter, such that, for example, the year labeled 1980 runs from July 1, 1980 to June 30, 1981.) Based on this definition, we consider 11 El Niño and 9 La Niña events between the years 1948 and 2015. We calculate the in-weighted degree fields for El Niño and La Niña by taking the average of the same type of events using

$$\text{IN}(C_i) = \sum_{y \in EY(LY)} \text{IN}(C^y_i)/S,$$
$$\text{IN}(W_i) = \sum_{y \in EY(LY)} \text{IN}(W^y_i)/S, \quad [5]$$

where $S = \sum_{y \in EY(LY)} I_i^y$, and EY and LY refer to the years (as defined above) in which El Niño and La Niña occur, respectively.

It is seen that regions affected by El Niño/La Niña, either by warming or cooling, such as North America (49), South America (50), Europe (51), India (52), South Africa (53, 54), and Australia (39), are characterized by relatively high in-weights (Fig. 1 *A*–*D*) and by high temperature anomalies (Fig. 1 *E* and *F*). The maps of temperature anomalies in Fig. 1 *E* and *F* are obtained by first calculating a 3-mo (December–February) mean temperature anomaly for each year, and then taking an average of the mean value over all El Niño/La Niña years. The El Niño/La Niña-related in-weighted extent fields are hemispherically symmetric, to some degree, in accordance with refs. 48 and 55.

In Table 1, we compare the in-weighted degree maps of El Niño/La Niña events with the corresponding temperature anomaly maps by evaluating the cross-correlation between each pair of maps shown in Fig. 1. Note that the different grid points are weighted by the cosine of the latitude, to account for the lower weights (due to the smaller area) at the higher latitudes. The cross-correlation values are found to be high, indicating the similarity between the different measures. For more detail, see *SI Appendix*, Tables S2 and S3. In addition, we also find that the averaged effects of El Niño and La Niña on different regions shown in Fig. 1 are quite similar. The cross-correlation value between Fig. 1 *A* and *B* is 0.54, indicating that El Niño and La Niña tend to affect similar regions.

Next, we study the variability of the regions that are influenced by El Niño/La Niña. We find that during El Niño/La Niña events, the overall global area that is influenced by the ENB becomes smaller, whereas the impacts in these more limited areas become stronger. This enhanced impact in localized regions is demonstrated in Fig. 2, which compares the global distributions of the in-degrees, IN(N); in-weights, IN(W); and IN(C), of typical El Niño and normal years. For IN(N), the differences are quite distinct—we see broader black regions (that indicate the absence of in-links), as well as broader dark red regions (that indicate that all links connected with the 57 grid points of the ENB are in-links), during El Niño years (Fig. 2*A*), compared with normal years (Fig. 2*B*). The underlying reason for this contrast is that, during El Niño, the temperatures of all 57 nodes located in the ENB are synchronized, such that for each influenced node outside the ENB, the 57 links with the ENB are more likely to have the same direction (i.e., outgoing from the ENB); this situation is less likely during normal years. We also find the localized phenomenon for in-weights, during El Niño years (Fig. 2 *C* and *E*), compared with normal years (Fig. 2 *D* and *F*). See also examples of cross-correlation functions for nodes inside and outside the ENB during El Niño in *SI Appendix*, Fig. S3.

A quantitative analysis of the area (number of nodes) that is affected/unaffected during El Niño and La Niña years is shown in Fig. 3, where El Niño and La Niña years are, respectively, emphasized by the red and blue shading. Here, the temporal evolution of the climate network is studied by constructing a sequence of networks based on successive windows of lengths of $365 + 200$ d, with a beginning date that is shifted by 1 mo each time. Fig. 3*A* depicts the ONI as a function of time. We focus on El Niño

Table 1. Comparison (using cross-correlation) between the in-weighted degree fields and the El Niño/La Niña mean winter temperature anomaly shown in Fig. 1

R	El Niño	La Niña
$R_{\mathrm{IN}(C),T}$	0.59	−0.55
$R_{\mathrm{IN}(W),T}$	0.54	−0.51
$R_{\mathrm{IN}(W),\mathrm{IN}(C)}$	0.92	0.95

See *SI Appendix*, Eqs. S1–S3 in the for the definition of R.

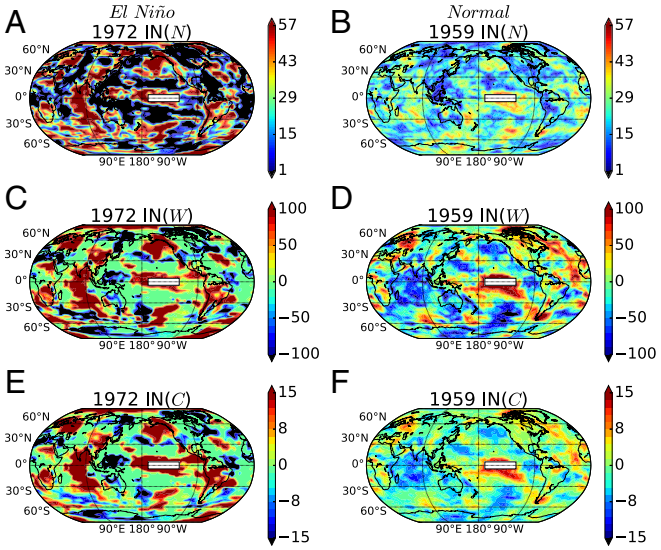

Fig. 2. The in-degree fields (N, W, and C) in a typical El Niño event, 1972 (*A*, *C*, and *E*), and a normal year, 1959 (*B*, *D*, and *F*).

(La Niña) events with ONIs that are larger (smaller) than 1°C (-1°C). Fig. 3*B* depicts the number of nodes with zero in-degree N^y as a function of time, and Fig. 3*C* depicts the average in-weights per node, which are given by dividing the sum of the absolute weights of all in-links of each node outside the ENB by N^y:

$$C^y = \sum_{i \notin ENB} \sum_{j \in ENB} A^y_{j,i} |C^y_{j,i}(\theta)| / N^y. \quad [6]$$

Fig. 3 shows the 3-mo running average of N^y and C^y.

It actually is seen that, during El Niño/La Niña, the number of nodes with no in-links, N^y, drops dramatically (Fig. 3*B*), indicating that the total area influenced by the ENB is much smaller. Moreover, during El Niño/La Niña, C^y increases significantly (Fig. 3*C*), indicating a stronger impact of the ENB in the areas that are influenced by it. We chose the 1982–1983 El Niño event to depict the evolution of ENSO impact, from its onset to its decay. We plot the in-weight maps every 3 mo (*SI Appendix*, Fig. S12). We find that, during the El-Nino event, the links are more localized in comparison with the beginning and the end of the event. To quantify the significance of the results, we used a randomization procedure in which we shuffled the years of each node's time series (keeping the time ordering within each year unchanged) and then constructed the in-weighted networks. We found that $C^y \geq 8$ and $N^y \leq 6300$ are significant with P values $<10^{-3}$. Other related network quantities are summarized in *SI Appendix*, Figs. S5–S7 and Table S1. The success of the climate-network-based measures to detect the El Niño/La Niña events strengthens the reliability of this approach in studying climate phenomenon.

It is possible to classify El Niño events based on the location of their maximum SST anomalies and on their tropical midlatitude teleconnections (56, 57). Here, we propose classifying different types of El Niño events based on the similarity between them, which can be determined by the cross-correlations between pairs of maps. We determine the significance of the cross-correlation using shuffled network maps. The shuffling is performed by dividing the map (globe) into 18 equal areas, shuffling their spatial orders for each event, and then evaluating the cross-correlation between each pair of the shuffled global network maps. Eventually, we obtain a distribution of the cross-correlation values through the shuffling process. Only correlations with P values <0.01 are considered as significant.

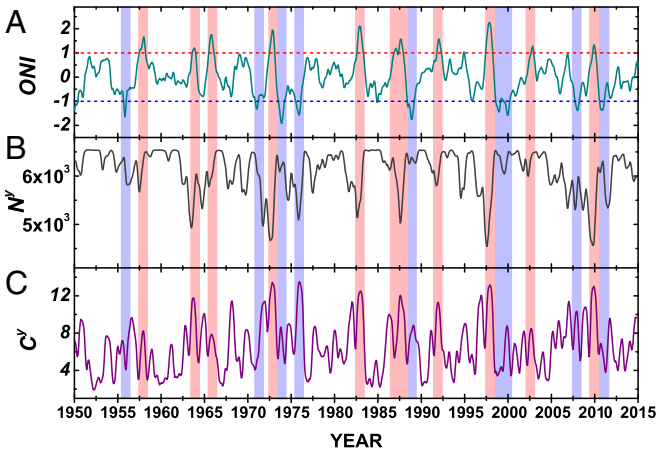

Fig. 3. (*A*) The ONI as a function of time. (*B*) The evolution of the number of nodes that have in-links with time. (*C*) The evolution of the average in-weights per node with time.

The cross-correlations between pairs of El Niño events is shown in Fig. 4*A*; insignificant cross-correlation is indicated by the white color. Based on this heat map, the 11 El Niño events are divided into three groups with extended white areas separating them, indicating that El Niño events within the same group tend to have similar global impact patterns. Furthermore, we divide the globe into three regions, approximately equal in area: "Tropics" (20°S to 20°N), "North" (20°N to 90°N), and "South" (20°S to 90°S). Then, separately for each region, we calculate the cross-correlations between the map pairs of the in-weighted climate network. The significant cross-correlations are also determined by P values <0.01, by shuffling the spatial orders of nodes within the same regions. The heat maps of cross-correlations for the different regions are shown in Fig. 4 *B*–*D*. We find that the global similarity structure receives different contributions from different regions. More specifically, the heat map for the Tropics region (Fig. 4*B*) is much more similar to the heat map for the global area (Fig. 4*A*), in comparison with the other two regions, indicating that the impact of El Niño in the tropics dominates the classification of El Niño events. We also construct the matrix of similarity of El Niño events based on the mean winter temperature anomaly and find that it is consistent with the network-based similarity structure (*SI Appendix*, Fig. S9).

A weighted network of the 11 El Niño years is also constructed based on the significant correlations given in Fig. 4*A* and is shown in Fig. 4*E*; the thickness of each link represents the correlation value between the two connected years. Then, by using a modularity optimization heuristic algorithm (58), our network is subdivided into three communities, which is consistent with the groups in Fig. 4*A*. To view the correlation patterns associated with each of the three communities, we chose three representative El Niño years (2009, 1986, and 1957), each from a different community. The in-weight maps are shown in *SI Appendix*, Fig. S11. The correlation patterns are quite different from each other; the correlation coefficients between them are summarized in Fig. 4*A*.

In summary, a general pattern of El Niño/La Niña's global impacts, as well as of their dynamical evolutions, are obtained from a time-evolving in-weighted climate network. By averaging the in-weighted degree fields of all significant El Niño/La Niña events, we identify the regions that tend to be more influenced by those events. One of the most important results of our study is that, during El Niño/La Niña periods, a smaller world area is affected by the ENB, but the impact of El Niño/La Niña is enhanced in these more localized regions. This observation is rooted in the fact that, during El Niño/La Niña, the entire ENB warms/cools; in addition, the regions that become warmer/cooler have similar/opposite tendencies with respect to the ENB. These synchronized behaviors enhance the overall correlation of the ENB with the rest of the world. However, during normal periods, part of the ENB is correlated and part is not, thus reducing the overall correlation and extending the regions of correlation.

The method proposed above enables the detection of local effects of each El Niño event; see *SI Appendix*, Fig. S10 for examples of climate networks of several El Niño and La Niña events. Evidently, these enhanced and localized El Niño effects are associated with serious consequences in many aspects of human life (59–62). In Fig. 1 *A* and *B*, we indicate (by arrows) three examples of regional effects of El Niño/La Niña discussed below. (*i*) Droughts and floods exacerbated by El Niño had directly affected East Africa, leading to an increase in food insecurity and malnutrition. El Niño had a varied significant impact on this region, ranging from floods affecting >3.4 million people during the 2006–2007 event to drought affecting >14 million people during the 2009–2010 event. Excessive rains during the 2014–2016 event have led to flooding in parts of Somalia, Kenya, Ethiopia, and Uganda, affecting nearly 410,000 people, displacing >231,900 people, and killing 271 people in the region (63). (*ii*) Agricultural output in India depends on the summer monsoons that are influenced by the timing, location, and intensity of El Niño. Some droughts in India have been accompanied by El Niño events (52). For example, the 2002–2003 El Niño event was accompanied by one of the worst Indian droughts in the past century, decreased the agricultural (cotton, oilseeds, and sugarcane) output, and led to food inflation (64). (*iii*) Precipitation in Australia had been associated with ENSO (38, 39), where El Niño (La Niña) tended to increase the risk of dry (wet) conditions across many parts of the continent (65). The 2010–2012 La Niña event was particularly important because it led to flooding across Australia and to the termination of the particular strong "Millennium Drought" (2001–2010) in eastern Australia (66).

The method we propose here enables the detection of the above regions as well as other regions across the globe that are affected by ENSO. See *SI Appendix*, Fig. S4 for typical cross-correlation functions during the specific El Niño events and regions described above.

The regions affected by El Niño vary from one El Niño event to another, making it difficult to predict the impacts of an upcoming El Niño. However, it is still possible to evaluate for each region (grid point) the probability to be affected by ENB by using

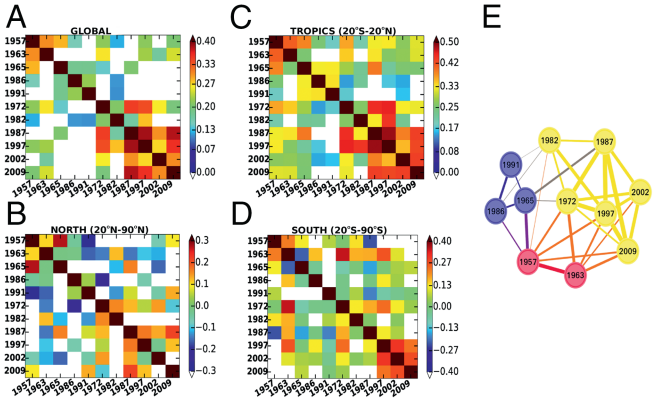

Fig. 4. The community structure of the 11 El Niño events. (*A*–*D*) The heat map of cross-correlations between pairs of El Niño events, based on the global (*A*), tropical (*B*), Northern Hemisphere (*C*), and Southern Hemisphere (*D*) maps of the in-weighted climate network. (*E*) Community structure in the network of 11 El Niño events. Different colors represent different communities.

our climate network approach. We define the frequency P_i for each node i in which the in-degrees I_i^y are nonzero. This P_i quantifies the probability effected by ENB. *SI Appendix*, Fig. S13 shows the spatial distribution of $P_i \geq 10$ (among 11 El Niño events); these regions are marked by red color (indicating probability $>> 90\%$) and include Australia (37–41), South Africa (42), southern South America (43), and Europe (44). El Niño phenomena can lead to warming or cooling in some regions, and the warming or cooling can be quantified by using $\mathrm{IN}(C_i^y)$–positive values for warming effects and negative values for cooling effects. *SI Appendix*, Fig. S14 *A* and *B* shows the spatial distribution of positive and negative $\mathrm{IN}(C_i^y)$ frequency, respectively. We find that some regions, such as Western North American, Western South America, South Indian, South Africa, and South Pacific, are very frequently and positively (warming) affected by El Niño; yet some regions, such as Southern South America and North Asian, are very frequently and negatively (cooling) affected (*SI Appendix*, Fig. S14). These results are consistent to some degree with the temperature anomalies during El Niño shown in Fig. 1*E*. To strengthen the above results, we also analyzed the frequency (during El Niño years) of the temperature anomalies to be above or below one SD of normal years (*SI Appendix*, Fig. S14 *C* and *D*). These results support the results obtained by using the network approach (compare *SI Appendix*, Fig. S14 *A–C* for warming and *SI Appendix*, Fig. S14 *B–D* for cooling) and can help to identify the regions that have the highest probability to be affected by El Niño.

Finally, according to our results, different El Niño events can drive different extreme weather conditions in different regions. For instance, the recently terminated El Niño event was distinct from most El Niño events in certain key aspects of climate disruptions (32). Collecting updated information is important in improving related models. Meanwhile, the detection of similarities between different El Niño events is also helpful in understanding important common aspects. We distinguish between different types of El Niño events based on the similarities between the networks of these events. According to our results, the similarities between different events are mostly due to the impacts of El Niño on Tropics (20°S to 20°N) compared with North (20°N to 90°N) and South (20°S to 90°S); the Tropics area is $\sim$1/3 of the global world area. The methodology and results presented here may help to improve the understanding of the impacts of ENSO, and hopefully to provide the ability, in the future, to take early actions to reduce the damage caused by El Niño. The mechanism underlying the results reported above is still not clear to us, and further study, maybe related to teleconnections, is needed to explore this mechanism.

ACKNOWLEDGMENTS. We thank Avi Gozolchiani for helpful discussions. This work was supported by MULTIPLEX EU (European Union) Project 317532; the Israel Science Foundation; the Israel Ministry of Science and Technology (MOST) with the Italy Ministry of Foreign Affairs; MOST with the Japan Science and Technology Agency; the Office of Naval Research; and the Defense Threat Reduction Agency. J.F. was supported by a fellowship program funded by the Planning and Budgeting Committee of the Council for Higher Education of Israel.

1. Watts D, Strogatz S (1998) Collective dynamics of 'small-world' networks. *Nature* 393:440–442.
2. Barabási A, Albert R (1999) Emergence of scaling in random networks. *Science* 286:509–512.
3. Brockmann D, Helbing D (2013) The hidden geometry of complex, network-driven contagion phenomena. *Science* 342:1337–1342.
4. Cohen R, Havlin S (2010) *Complex Networks: Structure, Robustness and Function* (Cambridge Univ Press, Cambridge, UK).
5. Newman M (2010) *Networks: An Introduction* (Oxford Univ Press, New York).
6. Tsonis AA, Swanson KL, Roebber PJ (2006) What do networks have to do with climate? *Bull Am Meteorol Soc* 87:585–595.
7. Tsonis AA, Swanson KL, Kravtsov S (2007) A new dynamical mechanism for major climate shifts. *Geophys Res Lett* 34:L13705.
8. Yamasaki K, Gozolchiani A, Havlin S (2008) Climate networks around the globe are significantly affected by El Niño. *Phys Rev Lett* 100:228501.
9. Donges JF, Zou Y, Marvan N, Kurths J (2009) Complex networks in climate dynamics. *Eur Phys J Spec Top* 174:157–179.
10. Donges JF, Zou Y, Marvan N, Kurths J (2009) The backbone of the climate network. *Europhys Lett* 87:48007.
11. Steinhaeuser K, Chawla NV, Ganguly AR (2010) An exploration of climate data using complex networks. *SIGKDD Explor* 12:25–32.
12. Steinhaeuser K, Chawla NV, Ganguly AR (2011) Complex networks as a unified framework for descriptive analysis and predictive modeling in climate science. *Statist Anal Data Min* 4:497–511.
13. Barreiro M, Marti AC, Masoller C (2011) Inferring long memory processes in the climate network via ordinal pattern analysis. *Chaos* 21:013101.
14. Deza J, Barreiro M, Masoller C (2013) Inferring interdependencies in climate networks constructed at inter-annual, intra-season and longer time scales. *Eur Phys J Spec Top* 222:511–523.
15. Ludescher J, et al. (2013) Improved El Niño forecasting by cooperativity detection. *Proc Natl Acad Sci USA* 110:11742–11745.
16. Ludescher J, et al. (2014) Very early warning of next El Niño. *Proc Natl Acad Sci USA* 111:2064–2066.
17. Donges JF, Schultz HCH, Marwan N, Zou Y, Kurths J (2011) Investigating the topology of interacting networks. *Eur Phys J B* 84:635–651.
18. Steinhaeuser K, Ganguly AR, Chawla NV (2012) Multivariate and multiscale dependence in the global climate system revealed through complex networks. *Clim Dynam* 39:889–895.
19. Guez O, Gozolchiani A, Berezin Y, Brenner S, Havlin S (2012) Climate network structure evolves with North Atlantic oscillation phases. *Europhys Lett* 98: 38006.
20. Guez O, Gozolchiani A, Berezin Y, Wang Y, Havlin S (2013) Global climate network evolves with North Atlantic Oscillation phases: Coupling to Southern Pacific Ocean. *Europhys Lett* 103:68006.
21. Wang Y, et al. (2013) Dominant imprint of Rossby waves in the climate network. *Phys Rev Lett* 111:138501.
22. Zhou D, Gozolchiani A, Ashkenazy Y, Havlin S (2015) Teleconnection paths via climate network direct link detection. *Phys Rev Lett* 115:268501.
23. Tsonis AA, Swanson KL (2008) Topology and predictability of El Niño and La Niña networks. *Phys Rev Lett* 100:228502.
24. Gozolchiani A, Havlin S, Yamasaki K (2011) Emergence of El Niño as an autonomous component in the climate network. *Phys Rev Lett* 107:148501.
25. Radebach A, Donner RV, Runge J, Donges JF, Kurths J (2013) Disentangling different types of El Niño episodes by evolving climate network analysis. *Phys Rev E* 88:052807.
26. Barrat A, Barthelemy M, Pastor-Satorras R, Vespignani A (2004) The architecture of complex weighted networks. *Proc Natl Acad Sci USA* 101:3747–3752.
27. Zemp DC, Wiedermann M, Kurths J, Rammig A, Donges JF (2014) Node-weighted measures for complex networks with directed and weighted edges for studying continental moisture recycling. *Europhys Lett* 107:58005.
28. Sarachik ES, Cane MA (2010 *The El Niño-Southern Oscillation Phenomenon* (Cambridge Univ Press, Cambridge, UK).
29. Dijkstra HA (2005) *Nonlinear Physical Oceanography: A Dynamical Systems Approach to the Large Scale Ocean Circulation and El Niño* (Springer Science, New York).
30. Dijkstra HA (2006) The ENSO phenomenon: Theory and mechanisms. *Adv Geosci* 6: 3–15.
31. Levine AFZ, McPhaden MJ (2016) How the July 2014 easterly wind burst gave the 2015-2016 El Niño a head start. *Geophys Res Lett* 43:6503–6510.
32. Kintisch E (2016) How a 'Godzilla' El Niño shook up weather forecasts. *Science* 352:1501–1502.
33. Giannini A, Chiang J, Cane MA, Kushnir Y, Seager R (2001) The ENSO teleconnection to the tropical Atlantic Ocean: Contributions of the remote and local SSTs to rainfall variability in the tropical Americas. *J Clim* 14:4530–4544.
34. Helbing D (2013) Globally networked risks and how to respond. *Nature* 497:51–59.
35. Halpert MS, Ropelewski CF (1992) Surface temperature patterns associated with the Southern Oscillation. *J Clim* 5:577–593.
36. Ropelewski CF, Halpert MS (1986) North American precipitation and temperature patterns associated with the El Nino/Southern Oscillation (ENSO). *Mon Weather Rev* 114:2352–2362.
37. Chiew FHS, Piechota TC, Dracup JA, McMahon TA (1998) El Nino/Southern Oscillation and Australian rainfall, streamflow and drought: Links and potential for forecasting. *J Hydrol* 204:138–149.
38. Power S, et al. (1999) Australian temperature, Australian rainfall and the Southern Oscillation, 1910-1992: Coherent variability and recent changes. *Aust Meteorol Mag* 47:85–101.
39. Power S, Casey T, Folland C, Colman A, Mehta V (1999) Inter-decadal modulation of the impact of ENSO on Australia. *Clim Dynam* 15:319–324.
40. Wang G, Hendon HH (2007) Sensitivity of Australian rainfall to inter-El Niño variations. *J Clim* 20:4211–4226.
41. Taschetto AS, England MH (2009) El Niño Modoki impacts on Australian rainfall. *J Clim* 22:3167–3174.
42. Reason CJC, Jagadheesha D (2005) A model investigation of recent ENSO impacts over Southern Africa. *Meteorol Atmos Phys* 89:181–205.

43. Magaña V, Ambrizzi T (2005) Dynamics of subtropical vertical motions over the Americas during El Niño boreal winters. *Atmósfera* 18:211–235.
44. Brönnimann S (2007) Impact of El Niño–Southern Oscillation on European climate. *Rev Geophys* 45:RG3003.
45. Klein SA, Soden BJ, Lau NC (1999) Remote sea surface temperature variations during ENSO: Evidence for a tropical atmospheric bridge. *J Clim* 12:917–932.
46. Kalnay E, et al. (1996) The NCEP/NCAR 40-year reanalysis project. *Bull Am Meteorol Soc* 77:437–471.
47. Dee DP, et al. (2011) The ERA-Interim reanalysis: Configuration and performance of the data assimilation system. *Q J R Meteorol Soc* 137:553–597.
48. Seager R, Harnik N, Kushnir Y (2003) Mechanisms of hemispherically symmetric climate variability. *J Clim* 16:2960–2978.
49. Cane MA (1998) A role for the tropical Pacific. *Science* 282:59–61.
50. Grimm AM, Barros VR, Doyle ME (2000) Climate variability in southern South America associated with El Niño and La Niña events. *J Clim* 13:35–58.
51. Fraedrich K, Müller K (1992) Climate anomalies in Europe associated with ENSO extremes. *Int J Climatol* 12:25–31.
52. Kumar KK, Rajagopalan B, Hoerling M, Bates G, Cane M (2006) Unraveling the mystery of Indian monsoon failure during El Niño. *Science* 314:115–119.
53. Baylis M, Mellor PS, Meiswinkel R (1999) Horse sickness and ENSO in South Africa. *Nature* 397:574–574.
54. Anyamba A, Tucker CJ, Mahoney R (2002) From El Niño to La Niña: Vegetation response patterns over East and Southern Africa during the 1997-2000 period. *J Clim* 15:3096–3103.
55. Seager R, et al. (2005) Mechanisms of ENSO-forcing of hemispherically symmetric precipitation variability. *Q J R Meteorol Soc* 131:1501–1527.
56. Ashok K, Behera SK, Rao SA, Weng H, Yamagata T (2007) El Niño Modoki and its possible teleconnection. *J Geophys Res* 112:C11007 .
57. Yeh SW, et al. (2009) El Niño in a changing climate. *Nature* 461:511–514.
58. Blondel VD, Guillaume JL, Lambiotte R, Lefebvre E (2008) Fast unfolding of communities in large networks. *J Stat Mech* 2008:P10008.
59. Hsiang SM, Meng KC, Cane MA (2011) Civil conflicts are associated with the global climate. *Nature* 476:438–441.
60. Schleussner CF, Donges JF, Donner RV, Schellnhuber HJ (2016) Armed-conflict risks enhanced by climate-related disasters in ethnically fractionalized countries. *Proc Natl Acad Sci USA* 113:9216–9221.
61. Burke M, Gong E, Jones K (2015) Income shocks and HIV in Africa. *Econ J* 125: 1157–1189.
62. Currie J, Rossin SM (2013) Weathering the storm: Hurricanes and birth outcomes. *J Health Econ* 32:487–503.
63. World Health Organization (2017) Emergency Events Database (EM-DAT) of the World Health Organization. Available at www.unocha.org/legacy/el-nino-east-africa. Accessed January 21, 2017.
64. Gadgil S, Rajeevan M, Nanjundiah R (2005) Monsoon prediction-why yet another failure? *Curr Sci* 88:1389–1400.
65. Power S, Haylock M, Colman R, Wang X (2006) The predictability of interdecadal changes in ENSO activity and ENSO teleconnections. *J Clim* 19:4755–4771.
66. Gergis J, et al. (2012) On the long-term context of the 1997–2009 'Big Dry'in South-Eastern Australia: Insights from a 206-year multi-proxy rainfall reconstruction. *Clim Change* 111:923–944.

Supporting Information: "Network analysis reveals strongly localized impacts of El Niño"

Jingfang Fan, Jun Meng, Yosef Ashkenazy, Shlomo Havlin and Hans Joachim Schellnhuber.

1. ENSO as a low frequency phenomenon of the global climate system

In this section, we discuss the global impact of El Niño and La Niña. We first demonstrate that ENSO is a low frequency phenomenon of the global climate system, typically occurring every 3-5 years. Following the main text, link weights are defined using the absolute values of $C^y_{i,j}(\theta)$ and $W^y_{i,j}$ [Eq. 1]. Here we construct only one network by evaluating the cross-correlation of each pair of global nodes, based on the whole range of the data set (i.e., between January 1948 and December 2015). For each grid point, the corresponding average link strength (using C and W) is calculated by dividing the total weights by the total number of links that connect the specific node to all the other nodes.

FIG. S1 (a) and (b) show that the high latitude regions tend to have lower C but higher W, while the low latitude areas are characterized by relatively high C and low W (1). How is this contrast formed? To answer this question, we calculate the ratio between the low frequency amplitude and the overall amplitude. The bright regions in FIG. S1 (c) correspond to the high ratio of low frequency components (with a cutoff at $f_c = 1/year$) in the Fourier transformation of each grid point's time series. It is clear that this ratio is higher in the low latitudes than in the high latitudes. Thus, the time series slowly vary in the low latitudes, compared to the high latitudes, resulting in a slowly varying cross-correlation function, C, which is also relatively high. The W measure, on the other hand, quantifies the contrast between the maximum value minus the mean value of the correlation values divided by the standard deviation, such that its value is small after the division by the relatively large standard deviation. We note that in the main text, only links outgoing from the ENB were considered, a fact that yielded the close correspondence between C and W shown in Fig. 1 and discussed in Table I of the main text.

In FIGs. S2 and S3, we show typical links between the ENB and a point outside the ENB (in the Sea of Okhotsk) [FIG. S2 (a)]. We find that the tendency of slow temporal evolutions of temperature, characterized by the cubic fit to the time series (dashed lines in FIG. S2 (b)), underlies the slowly varying cross-correlation function C and the high value of positive maximal C [FIG. S3 (a)]; an opposite tendency [FIG. S2 (c)] yielded the high value of negative minimal C [FIG. S3 (c)]. These results are further demonstrated by the fact that after the removal of the low frequency components in the time series shown in FIG. S2 (b) and (c), the high correlation shown in FIG. S3 (a) vanished. Furthermore, from the example of FIGS. S2 and S3, we find that the ENB can influence the same remote region in opposite ways, in which sometimes it is associated with warming [FIG. S2 (b)] and sometimes with cooling [FIG. S2 (b)].

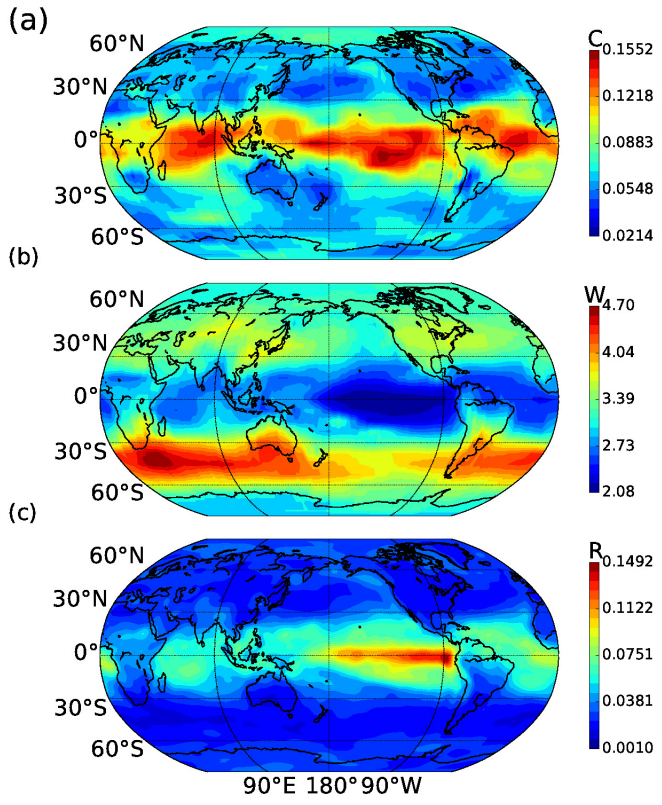

Fig. S1. (a) The spatial distribution of average link strength C. (b) The spatial distribution of average link strength W. (c) The ratio between the amplitude of the low frequency components ($f_c < 1/year$) and the total amplitude. A fourier transform is used to obtain this figure.

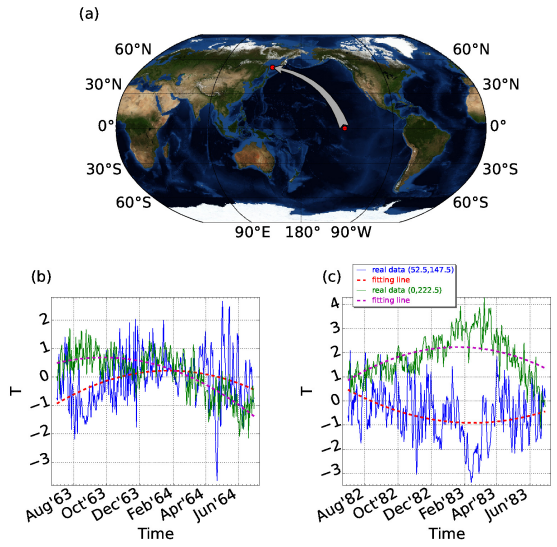

Fig. S2. (a) Example of an "in"-link, from the ENB to the Sea of Okhotsk. (b) The temporal evolutions of the temperature anomaly (in °C) of the two points shown in (a), from July 1963 to June 1964. The dashed lines are the cubic fit of the temperature anomaly time series. (c) Same as (b) for the time period from July 1982 to June 1983.

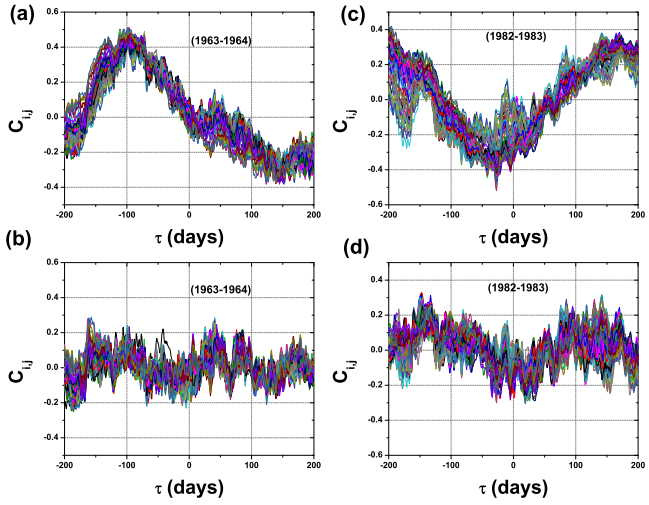

Fig. S3. (a) The cross-correlation functions between the ENB and a point outside the ENB (shown in FIG. S4 (a)), for the 1963-1964 El Niño event. The cross-correlation functions indicate positive correlations. (b) Same as (a) but for the detrended time series (i.e., the original time series minus the cubic fit of the time series). (c) Same as (a) for the 1982-1983 El Niño event. The cross-correlation functions indicate negative correlations. (d) Same as (b) for the 1982-1983 El Niño event.

2. "in"-link examples from the ENB

In FIG. S4, we show the cross correlation function of three typical "in"-link examples which demonstrated in Fig. 1 (a).

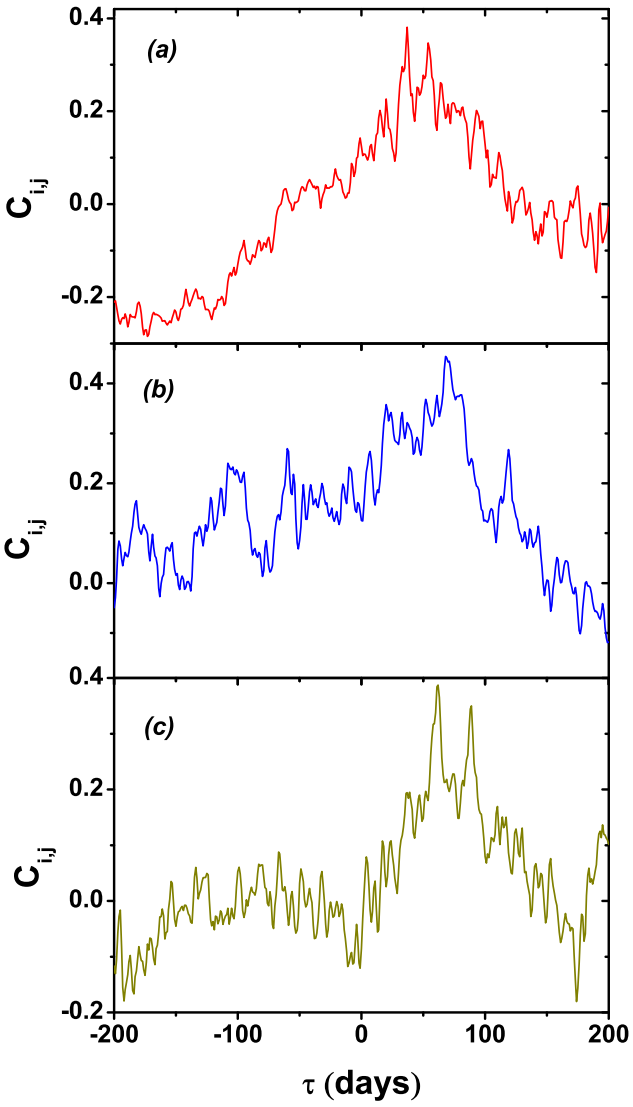

Fig. S4. The cross correlation function for three "in"-link examples from the ENB (which are mentioned in Fig. 1 (a) and (b)). (a) From the ENB to Chicualacuala in Mozambique during 2009-2010 El Niño event; (b) from the ENB to Rambaxpura in India during 2002-2003 El Niño event; (c) from the ENB to Jundah in Australia during 2010-2011 La Niña event.

3. Dynamical behavior of the "in"-weighted climate network

In FIG. 3 of the main text, we depict the temporal evolution of the climate network system. Here we present additional network-based quantities, similar to the main text; see FIGS. S5 to S7. The similarity between the different measures and ONI is summarized in Table S1. Our analysis is based on

two different datasets, the NCEP (2) and the ERA-Interim (3).

Using the same methods described in the main text, we constructed time-evolving climate networks based on the ERA-Interim reanalysis data. In FIG. S5, we show that this dataset yielded similar results to those presented in Fig. 3 of the main text, i.e., the number of nodes with no zero "in"-degrees, N^y, [FIG. S5 (b)] decreased, and the average "in"-weights per node C^y [FIG. S5 (c)] increased, during El Niño and La Niña events.

Next, we analyzed several network quantities based on the NCEP [FIG. S6] and ERA-Interim [FIG. S7] reanalysis data. According to our results, during El Niño or La Niña, the standard deviation of the number of "in"-links per node, $std(N^y)$, increased [FIG. S6 (b) and FIG. S7 (b)], indicating that the distribution of "in"-degrees are more localized; the number of "in"-links in the top 15%, $N^y(top15\%)$, increased [FIG. S6 (c) and FIG. S7 (c)], indicating that regions influenced by the ENB tend to have more "in"-links. The sum of the absolute weights of all "in"-links of each node outside the ENB, C_T^y, increased [FIG. S6 (d) and FIG. S7 (d)], indicating that the ENB has a stronger impact on the globe. The average "in"-weights per link, C_L^y, obtained by dividing C_T^y by the total number of "in"-links, increased [FIG. S6 (e) and FIG. S7 (e)], indicating that the impact of each node inside the ENB is enhanced in regions that are influenced by El Niño.

In Table S1, we present the cross-correlation between the time series of network quantities shown in FIGS. S5 to S7 and the ONI. We find that the 6th column in Table S1, referring to the average "in"-weights per node C^y, defined in the main text using Eq. 5, best correlates to the temperature.

Next we analyzed measures based on the link strength $W_{i,j}^y$, defined in Eq. (1) of the main text. Similar to C_T^y, C^y and C_L^y defined in the previous paragraphs, we defined W_T^y, W^y and W_L^y; these measures do not significantly correlate with the ONI. Actually, during El Niño events, the link strength becomes lower than in normal periods (4), which can be explained as follows. During El Niño (or La Niña), the low frequency components in the ENB and in locations that are influenced by the ENB become dominant, and hence, the cross-correlation function varies slowly, resulting in a lower link strength $W_{i,j}^y$ (as the standard deviation of the cross-correlation function becomes larger). However, for each node outside the ENB, if we only take into account the "in"-going links (i.e., the links that are "out"-going from the ENB), as we did in the main text, the link strength $W_{i,j}^y$ is still relatively higher in the regions that are influenced by the ENB than in regions that are not [Fig. 1 in the main text].

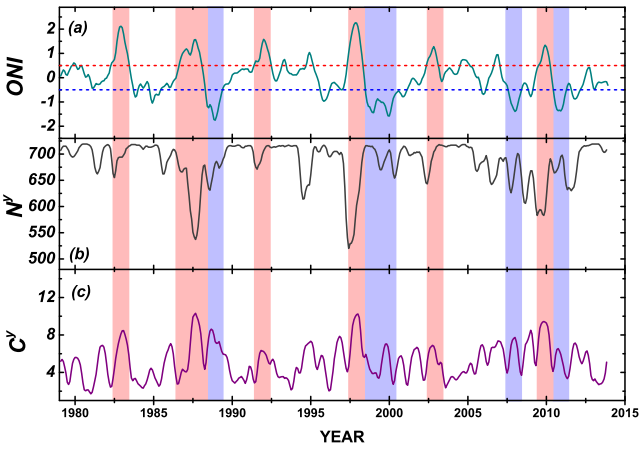

Fig. S5. Time evolution of the network measures based on the ERA-Interim reanalysis data (similar to Fig. 3 of the main text). (a) The Oceanic Niño Index (ONI). (b) The number of nodes that have "in"-links. (c) The average "in"-weights per node.

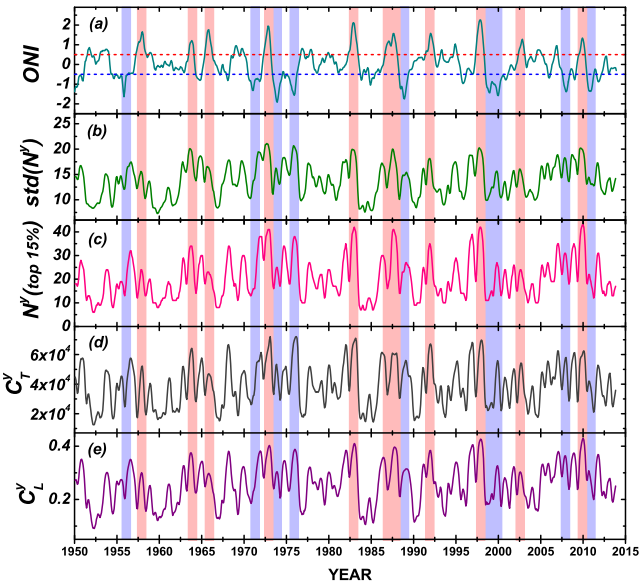

Fig. S6. Temporal evolution of network measures that are based on the NCEP reanalysis data. (a) The Oceanic Niño Index (ONI). (b) The standard deviation of the number of "in"-links of each node. (c) The number of "in"-links in the top 15%. (d) The total "in"-weights of all nodes. (e) The average "in"-weights per link.

4. "In"-weighted climate network

In this section, we discuss the robustness of our results. Firstly, we show that we obtained similar results when using another reanalysis dataset, the

R	N			C			W		
	node number	top 15%	STD	total	node	link	total	node	link
NCEP	-0.47	0.48	0.49	0.46	0.50	0.49	-0.29	0.34	-0.31
ERA	-0.53	0.50	0.51	0.51	0.55	0.52	0.27	0.37	0.21

Table S1. Values of the cross-correlations at zero time lag between the time series of different network quantities and the ONI. In the first row, N, C and W refer to quantities related to: "in"-degree, and "in"-weights $C^y_{i,j}$ and $W^y_{i,j}$. More specifically, in the second row, "node number" refers to N^y; "top 15%" refers to $N^y(top15\%)$; "STD" refers to $std(N^y)$; and "total", "node" and "link" correspond to the total "in"-weights C^y_T (or W^y_T), the average "in"-weights per node C^y (or W^y), and the average "in"-weights per link C^y_L (or W^y_L), respectively.

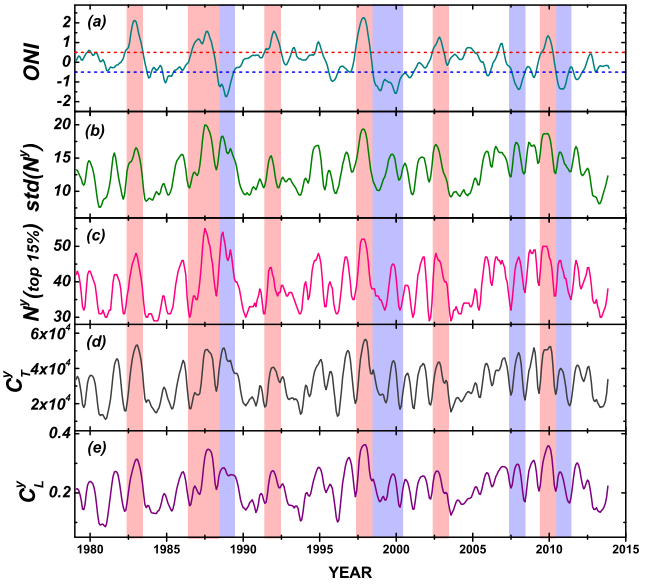

Fig. S7. Same as FIG. S6 for the ERA-Interim reanalysis data.

ERA-Interim; this is addition to the previous section. The network structure for El Niño [FIG. S8 (a) (c)] and La Niña [FIG. S8 (b) (d)] are similar to those presented in Fig. 1 of the main text.

Next, we demonstrate that our "in"-weighted climate network is more effective in describing El Niño and La Niña impacts than "out"-weighted networks. We quantified the similarity between maps of the weighted networks and the temperature anomaly using cross-correlations. The cross-correlations of two maps were calculated by converting each map to a vector with $n = 10455$ indices. Nodes located in the ENB were excluded. To take into account the smaller area of each grid point at higher latitudes, we defined the cross-correlation function as

$$R = \frac{\sum_{i=1}^{N}(C_i - \langle C\rangle)(T_i - \langle T\rangle)\cos(\lambda_i)}{\sqrt{\sum_{i=1}^{N}(C_i - \langle C\rangle)^2\cos(\lambda_i)}\sqrt{\sum_{i=1}^{N}(T_i - \langle T\rangle)^2\cos(\lambda_i)}} \quad [S1]$$

where i refers to the labels of the nodes taken into consideration, and $\langle\cdot\rangle$ indicates the average over all the nodes, C_i, T_i and λ_i refer to the "in"-weights, the temperature anomaly and the latitude of node i, respectively, and the $\langle\cdot\rangle$ is calculated using

$$\langle C\rangle = \frac{\sum_{i=1}^{N} C_i\cos(\lambda_i)}{\sum_{i=1}^{N}\cos(\lambda_i)}, \quad [S2]$$

$$\langle T\rangle = \frac{\sum_{i=1}^{N} T_i\cos(\lambda_i)}{\sum_{i=1}^{N}\cos(\lambda_i)}. \quad [S3]$$

In Tables S2 and S3, we list the cross-correlation values between the "in"-weighted degree field and the mean winter temperature anomaly and the cross-correlation values between the "out"-weighted degree field and the mean winter temperature anomaly. This is shown both for El Niño and La Niña. The correlation of the "in"-weighted network and the temperature is larger than the "out"-weighted network values. All values are significant with p-values lower than 0.01 (i.e., the observed correlations are higher than 100 cross-correlation values of shuffled data). The shuffling procedure is performed by dividing the map (globe) into 18 regions of equal area and then shuffling their spatial orders.

We also find a similar community structure of El Niño events by using mean winter temperature anomalies. To obtain the similarities of temperature between each pair of El Niño events, we perform scalar products by characterizing temperature anomalies for each grid point by 1 or -1, depending on whether it is positive or negative. FIG. S9 (a) and (b) show the community structures of 11 El Niño events based on network and temperature, respectively. Here we only consider pairs of years that are significant, for the network, with p-values smaller

than 0.01, and for the temperature, with p-values smaller than 0.05.

Next, we consider these significant values for both network and temperature. In FIG. S9, we show heat maps of significant similarities between pairs of El Niño events for both the "in"-weighted climate network [FIG. S9 (c)] and the mean winter temperature anomaly [FIG. S9 (d)]. The cross-correlation between the two heat maps is 0.41, with quite a low p-value of 0.034, compared with the shuffled data, which is performed by shuffling the order of the values.

From FIG. S9, we see that the community structure of the 11 El-Niño events are determined by excluding all insignificant values. Compared to [Fig. 4] in the main text, we find that the events in the largest group are the same (i.e., the same calendar years in the community); the only difference is that the $1965-1966$ event departs from the $1986-1987$, $1991-1992$ group, and merges into the $1957-1958$ and $1963-1965$ components in this case.

At last, we show examples of climate network for El-Niño 1997 and La Niña 1988 in FIG. S10. By using our new method, we are able to detect and quantify the local impacts of each El-Niño/La Niña events.

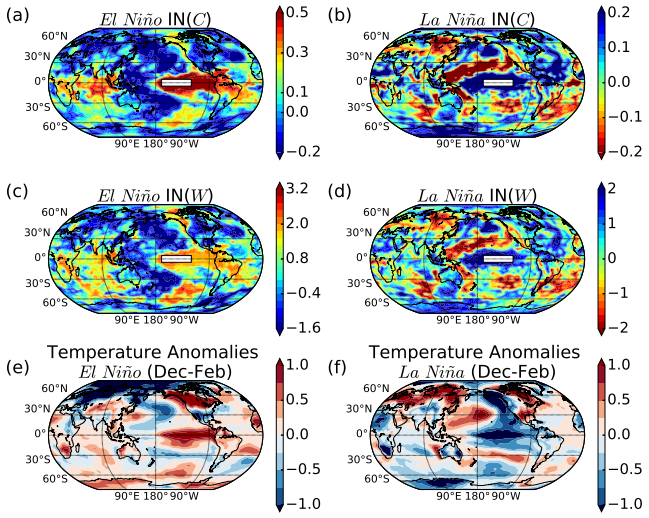

Fig. S8. (a), (c) "In"-weight maps (using C and W) for El Niño events. (b),(d) "In"-weight maps (using C and W) for La Niña events. (e), (f) Mean winter (Dec-Feb) temperature anomaly during El Niño and La Niña. All maps are obtained by using the ERA-Interim reanalysis dataset.

1. Guez O, Gozolchiani A, Havlin S (2014) Influence of autocorrelation on the topology of the climate network. *Phys Rev E* 90(6): 062814.
2. Kalnay E, et al. (1996) The NCEP/NCAR 40-year reanalysis project. *Bull Am Meteorol Soc* 77(3): 437-471.
3. Dee DP, et al. (2011) The ERA-Interim reanalysis: Configuration and performance of the data assimilation system. *Quarterly Journal of the royal meteorological society* 137(656): 553-597.

R	El-Niño		La-Niña	
	IN	OUT	IN	OUT
$R_{T,C}$	0.59	0.34	-0.55	-0.34
$R_{T,W}$	0.54	0.31	-0.51	-0.33
$R_{C,W}$	0.92	0.93	0.0.95	0.94

Table S2. Cross-correlation between "in"/"out"-weight maps and the mean winter temperature anomaly, based on the NCEP reanalysis dataset.

R	El-Niño		La-Niña	
	IN	OUT	IN	OUT
$R_{T,C}$	0.45	0.23	-0.42	-0.16
$R_{T,W}$	0.40	0.23	-0.36	-0.16
$R_{C,W}$	0.91	0.92	0.94	0.93

Table S3. Same as TABLE. S2 for the ERA-Interim reanalysis dataset.

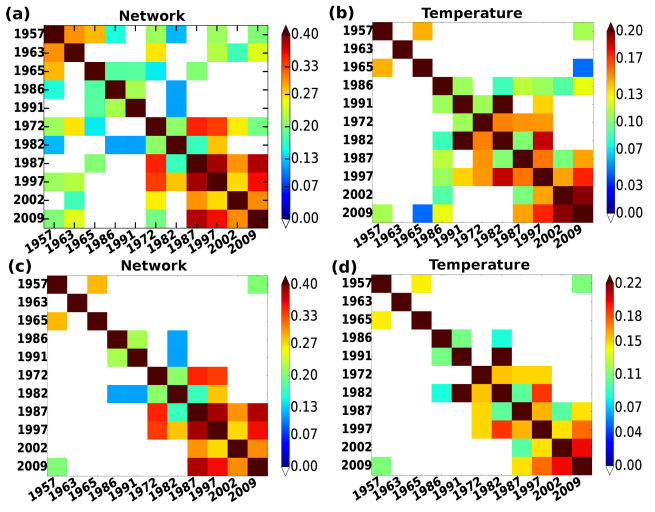

Fig. S9. The community structure of 11 El Niño events, (a) The heat map of cross-correlations between pairs of El Niño events, based on the global maps of the "in"-weighted climate network. Here, only significant values with p-values no larger than 0.01 are included. (b) The heat map of normalized scalar products between pairs of El Niño events, based on the global maps of the mean winter temperature anomaly. Here, only significant values with p-values no larger than 0.05 are included. (c) The heat map of cross-correlations between pairs of El Niño events, based on the global maps of the "in"-weighted climate network. Here, only pairs of years that are significantly similar in both the network structure and the temperature are included. (d) The heat map of normalized scalar products between pairs of El Niño events, based on the global maps of the mean winter temperature anomaly. Here, only pairs of years that are significantly similar in both the network structure and the temperature are included.

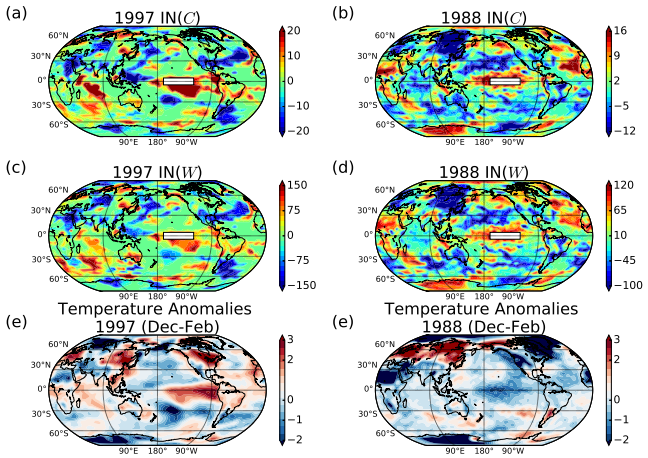

Fig. S10. (a), (c) "In"-weight maps (using C and W) for El Niño 1997. (b),(d) "In"-weight maps (using C and W) for La Niña 1988. (e), (f) Mean winter (Dec-Feb) temperature anomaly during El Niño 1997 and La Niña 1988.

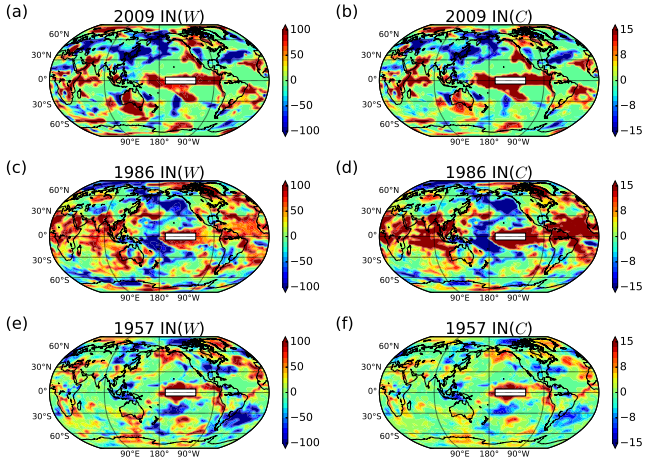

Fig. S11. "In"-weight maps for three typical El Niño years selected by three communities.

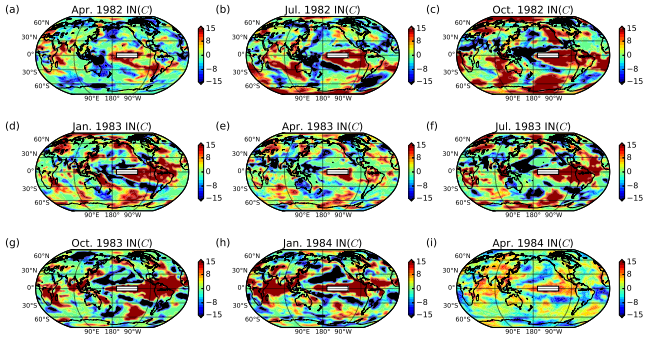

Fig. S12. The evolution of ENSO impact for a special El Niño event (1982) from onset to withdrawal.

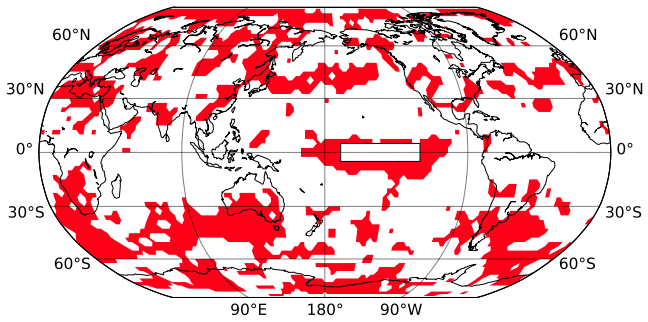

Fig. S13. The spatial distribution of frequency P_i for each node i. The regions marked by red color have high probability (at least 10 over 11) effected by El Niño.

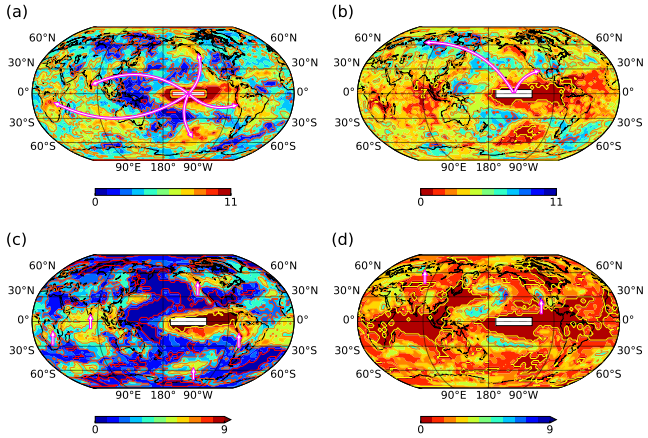

Fig. S14. The spatial distribution of positive (a) and negative (b) $\mathrm{IN}(C_i^y)$ frequency; the frequency for the temperature anomalies are above one standard deviation (c), and below minus one standard deviation (d) of normal years.

4. Yamasaki K, Gozolchiani A, Havlin S (2008) Climate networks around the globe are significantly affected by El Niño. *Phys Rev Lett* 100(22): 228501.